Unravelling Thermal and Enthalpy Evolutions of Commercial Sodium-Ion Cells upon Cycling Ageing via Fiber Optic Sensors

Jiaqiang Huang, Charles Delacourt, Parth Desai, Charlotte Gervillié-Mouravieff, Laura Albero Blanquer, Ruifeng Tan, Jean-Marie Tarascon

To cite this version:

Jiaqiang Huang, Charles Delacourt, Parth Desai, Charlotte Gervillié-Mouravieff, Laura Albero Blanquer, et al.. Unravelling Thermal and Enthalpy Evolutions of Commercial Sodium-Ion Cells upon Cycling Ageing via Fiber Optic Sensors. Journal of The Electrochemical Society, 2023, 170 (9), pp.090510. 10.1149/1945-7111/acf625 . hal-04220590

HAL Id: hal-04220590
https://u-picardie.hal.science/hal-04220590v1

Submitted on 19 Nov 2024

Journal of The Electrochemical Society

The Electrochemical Society
Advancing solid state & electrochemical science & technology

Unravelling Thermal and Enthalpy Evolutions of Commercial Sodium-Ion Cells upon Cycling Ageing via Fiber Optic Sensors

To cite this article: Jiaqiang Huang *et al* 2023 *J. Electrochem. Soc.* **170** 090510

Journal of The Electrochemical Society, 2023 **170** 090510

Unravelling Thermal and Enthalpy Evolutions of Commercial Sodium-Ion Cells upon Cycling Ageing via Fiber Optic Sensors

Jiaqiang Huang,[1,2,3,4] Charles Delacourt,[4,5] Parth Desai,[1,4,6] Charlotte Gervillié-Mouravieff,[1,4] Laura Albero Blanquer,[1,4,6] Ruifeng Tan,[2] and Jean-Marie Tarascon[1,4,6,z]

[1]*Collège de France, Chimie du Solide et de l'Energie—UMR 8260 CNRS, Paris, France*
[2]*The Hong Kong University of Science and Technology (Guangzhou), Sustainable Energy and Environment Thrust and Guangzhou Municipal Key Laboratory of Materials Informatics, Nansha, Guangzhou, Guangdong 511400, People's Republic of China*
[3]*HKUST Shenzhen-Hong Kong Collaborative Innovation Research Institute, Futian, Shenzhen, Guangdong, People's Republic of China*
[4]*Réseau sur le Stockage Electrochimique de l'Energie (RS2E), CNRS FR 3459, Hub de l'Energie, Rue Baudelocque, 80039 Amiens Cedex, France*
[5]*Laboratoire de Réactivité et Chimie des Solides (LRCS), CNRS UMR 7314, Université de Picardie Jules Verne, Hub de l'Energie, Rue Baudelocque, 80039 Amiens Cedex, France*
[6]*Sorbonne Universit´e, Paris 75005, France*

Battery ageing is inevitable for chemistry of any kind and still occupies a central place in battery research and development. However, the operando monitoring of battery ageing under real working conditions remains largely unexplored. Herein, we demonstrate the feasibility of using fiber Bragg grating sensors to operando monitor the thermal (temperature and heat) evolutions of commercial 18650 sodium-ion cells during long-term cycling ageing. With the delicate heat deconvolution, the evolutions of entropy and overpotential heat rates upon the cycling ageing are decoded, while the ageing-driven changes in overpotential components are further analysed. Drawing also on thermodynamics, high-resolution enthalpy profiles are computed from operando heat and voltage profiles, enabling to track and unravel redox variations during the cycling ageing. Collectively, this work shows that fiber optic sensors are essential tools for operando deciphering cell ageing and offer tremendous opportunities for academia and industry alike.

[DOI: 10.1149/1945-7111/acf625]

Manuscript submitted June 11, 2023; revised manuscript received July 27, 2023. Published September 11, 2023.

Supplementary material for this article is available online

Batteries are at the heart of transportation electrification and the transition from fossil fuels to a carbon-neutral future.[1] Long after the invention of the voltaic pile near 1800, the great prosperity of batteries came with the commercialization of lithium-ion technologies in 1991 and the growing markets[2] of portable electronics, electric vehicles (EVs), personal mobility, and grid applications. Due to the scarcity of lithium reserves[3] and the recent spike in lithium precursor prices, sodium-ion batteries have recently emerged as a complementary,[4] turnkey alternative.

Ageing is inevitable, regardless of the battery's chemistry. Monitoring cell ageing and determining cell health is paramount, not only for the battery management system (BMS) and the second life of batteries but also for the design of better batteries. However, the diagnostics and prognosis of ageing are not trivial due to the complex and intertwined ageing mechanisms,[5] including the thickening of solid electrolyte interphase (SEI) arising from electrolyte degradation, the metal plating, the loss of electronic contacts within the electrode and at the collector/electrode interface, and the deterioration of material structures. Many techniques, such as X-ray and transmission electron microscopy (TEM), are extremely useful in studying these mechanisms. However, most of these techniques cannot operando follow long-term cell ageing, as they remain ex situ or in situ. Even for in situ monitoring, these sophisticated techniques are mainly applied to customized cells, and operando tracking the long-term behaviours of real commercial cells remains a challenge. Therefore, there is an urgent need to develop operando diagnostic tools to monitor commercial cell ageing in a timely manner, which will provide a better understanding of how and why cells age.

Starting from the basics, electrochemical methods[5] are powerful to sense cell ageing, relying on time-domain voltage, current, and frequency-domain impedance. To understand the cell de-balancing and diagnose ageing phenomena, coulometry[6] (e.g., coulombic counting and coulombic efficiency) and derivative methods[7] (e.g., dQ/dV and dV/dQ) are frequently deployed, providing quantified information on secondary reactions and allow estimation of active material loss. Turning to the field applications, voltage and current are often fed into the onboard BMS to determine the model parameters (such as resistances and capacitances) of the equivalent circuit model (ECM) for estimating the cells' state of health (SOH). ECM methods offer reasonable performance at an acceptable computational cost and are, therefore, widely used in field applications (e.g., EVs and stationary energy storage). However, batteries are complex physiochemical systems, and the over-simplification of ECM often leads to multiple solutions, requiring additional physical constraints.

Additional physical information is usually provided by sensors. For instance, thermocouples or thermistors are placed on the module or sub-module level to record temperature changes. In addition to these conventional sensors, increasing research efforts have been made along this direction. Dahn et al. applied acoustic sensors to map the electrolyte depletion upon ageing.[8,9] Also, Dahn et al. used strain sensors to monitor the SEI-induced pressure build-up with cycling ageing.[10] Alternatively, we have recently demonstrated that fiber optic sensors have great potential in battery diagnostics,[11] due to their hair-thin size, immunity to electromagnetic interference, and diverse capabilities to measure temperature,[12–17] heat,[12] pressure,[12] strain,[15,18] refractive index,[19] turbidity,[19] and infrared fingerprints[20] inside batteries. Regarding cell ageing, Ganguli et al. used fiber Bragg grating (FBG) sensors to track strain over approximately 100 cycles and found a nice correlation between strain and SOH.[21] Besides, our group also implemented a tilted fiber Bragg grating (TFBG) to operando monitor the electrolyte's refractive index and turbidity variations upon ageing and showed their strong correlations with the capacity retention.[19] It is worth noting that temperature

[z]E-mail: jean-marie.tarascon@college-de-france.fr

largely influences battery ageing[22] by varying mass transport, parasitic reaction kinetics, metal plating (favored at low temperatures), etc. However, surprisingly, the thermal evolutions of temperature and heat during cell ageing remain largely unexplored, not to mention their importance for the thermal management system.

To close this gap, herein, the $Na_3V_2(PO_4)_2F_3$/hard carbon (NVPF/HC) 18650 commercial sodium-ion cells are taken as the model system, and the FBG sensors are injected into the cells for monitoring the thermal dynamics during cycling ageing for at least 200 cycles. How the temperature and heat accumulate with the number of cycles is further quantified. In addition, the thermodynamic state function of enthalpy from non-equilibrium measurements is further exploited to uncover the origins of ageing. Lastly, the superiority of our fiber-based enthalpy potential methods is demonstrated by comparing the derivatives of enthalpy potential, voltage, and equilibrium upon cycling ageing at a high C-rate.

Experimental

Electrolyte and cell preparation.—The NVPF/HC 18650 cells were kindly provided by TIAMAT company (France). The 18650 cells were hermetically sealed without filling the electrolyte in the factory. The electrolyte used for 18650 cells contains 1 M $NaPF_6$ in ethylene carbonate (EC) and dimethyl carbonate (DMC) (v.:v. = 1:1) with 3 wt% vinylene carbonate (VC), 3 wt% succinonitrile (SN), 0.5 wt% sodium (oxalate) difluoro borate (NaODFB), and 0.2 wt% tris(trimethylsilyl) phosphite (TMSPi). All the solvents used for the electrolyte preparation were dried over molecular sieves for at least three days, and a water content of less than ten ppm was confirmed. Salts were dried at 80 °C in a Buchi oven under vacuum and transferred in the glovebox without exposure to the air.

FBG sensors.—The FBG sensors were inscribed in single-mode silica fibers and supplied by SAMYON company (China). All these sensors were calibrated before the implementation; see more details in our previous work.[12]

Internal sensor integration.—The integration of FBG sensors into 18650 cells was exactly the same as we did in previous work.[12,19] Namely, we drilled a hole of 0.8 mm diameter in the center of the negative pole of 18650 cells without electrolyte. The cells were then dried in a vacuum oven at 80 °C overnight before being transferred into an Ar-filled glove box, where 5.5 ml of electrolyte was injected into the electrolyte through the as-drilled 0.8 mm hole. Afterward, the FBG sensor was inserted into the central void of the jelly roll through the 0.8 mm hole and sealed with epoxy.

Electrochemical measurements.—The 18650 and coin cells were tested by BCS-815 potentiostat (Bio-Logic, France) in a temperature-controllable oven (Memmert, Germany).

Cycling ageing protocol.—The NVPF/HC 18650 cells were formed at C/10 (1 C = 128 mA g_{NVPF}^{-1}) for 3 cycles and then cycled at 1 C with a constant current—constant voltage (CC-CV, CV to C/5) charging scheme in a 55 °C temperature chamber. The voltage window was set between 2.0 V and 4.25 V. The diagnostic cycles, including the galvanostatic intermittent titration technique (GITT) and a 5C discharge, were performed mostly every 20 cycles, except for the initial ones.

Interrogation of FBG sensors.—The FBG sensors were interrogated by Si255 (Micron Optics, U.S.) with a wavelength accuracy and resolution of 1 pm. The acquisition time was set as 1 Hz.

Optical fiber calorimetry.—The experimental setup and calibrations were the same as our previous work.[12] To assess temperature and heat variations with cell ageing, one FBG inscribed on a single-mode fiber was inserted into the central void of NVPF/HC 18650 cells to detect only the internal temperature ($T_{internal}$) and to minimize the cross-sensitivity of strain and pressure, see more detailed rationales in our previous work.[12,19] Two FBG sensors were attached at the surfaces of the cell and the testing cabinet, respectively, for measuring the cell's surface temperature ($T_{surface}$) and the ambient temperature ($T_{ambient}$). These temperatures were extracted from the FBG signals by the general equation ($\Delta T = k_T \Delta\lambda$, where ΔT is the temperature variation, k_T is the FBG's temperature rate constant, which was calibrated before the experiments,[12] $\Delta\lambda$ is the wavelength variation of the Bragg peak of FBG being measured by the interrogator, LUNA Si255). With these three (internal, surface, and ambient) temperatures, a simplified zero-dimensional thermal model[23] was adopted to compute the time-resolved heat generation rate ($\dot{Q}$) of the cells, by the equation:

$$\dot{Q} = MC_P \frac{dT}{dt} + \frac{T_{surface} - T_{ambient}}{R_{out}} \quad [1]$$

where M is the cell's mass, C_P is the specific heat capacity, T is the spatial average temperature of the cell calculated[12] by $T_{internal}$ and $T_{surface}$ together with the cell geometry, t is the time, and R_{out} is the equivalent thermal resistance between the cell's surface and the ambient surrounding. Among these parameters, MC_P and R_{out} were determined by the transient and steady states during the thermal pulses, which was previously reported[12,23] and elaborated as follows. Namely, a 2A-current pulse at 2 Hz was implemented on the cells for 3 h to generate the heat that could be computed, that is, $\dot{Q} = \oint_{cycle} IV$, where I and V represent current and voltage, respectively. The current of 2 A was selected to generate largely enough temperature change, while the frequency of 2 Hz was chosen according to the previous paper.[23] Meanwhile, 3 h were selected to make sure the cells' temperature could reach the thermal steady state after the transient state.[12] At the thermal steady state, the temperature did not change and $\frac{dT}{dt} = 0$ so that R_{out} can be determined because $\dot{Q}$, $T_{surface}$, and $T_{ambient}$ were known in Eq. 1. Coming back to the transient-state data, only MC_P was currently unknown in Eq. 1 and could be determined then. Note that MC_P was assumed to be constant within the temperature range of the measurement. By doing so, the heat evolutions of the cells could be computed according to Eq. 1 for operando monitoring.

In addition to the time-resolved heat generation rate ($\dot{Q}$), we also went one step further to decompose $\dot{Q}$ into the reversible entropy heat rate $\left(\frac{IT}{nF}\left(\frac{ds_+}{dx} - \frac{ds_-}{dx}\right)\right)$ and the irreversible overpotential heat rate ($I(V - U)$) according to the following equation,[24–26] which ignores the heat of mixing:

$$\dot{Q} = I(V - U) + \frac{IT}{nF}\left(\frac{ds_+}{dx} - \frac{ds_-}{dx}\right) + \dot{q}_P \quad [2]$$

where U represents the equilibrium potential, n represents the electron number involved in the electrochemical reaction, F represents the Faraday's constant, $\frac{ds_+}{dx}$ and $\frac{ds_-}{dx}$ represent the change rates of the entropy per site over the fraction of filled sites of the positive and negative electrodes, respectively,[24–26] $\dot{q}_P$ represents the parasitic heat rate. In Supplementary Note 1, the magnitude of parasitic heat (ca. 0.04 and −0.79 mW g_{NVPF}^{-1} for C/5 and 1 C, respectively) was estimated, demonstrating that the parasitic heat could be reasonably ignored for the following discussion.

Results

Temperature variation with cycling ageing.—The voltage vs capacity curves at 1 C upon ageing (colour from purple to red) were plotted in Fig. 1a. The capacity at the higher-voltage plateau decayed much less than the one at the lower voltage plateau, as evident from

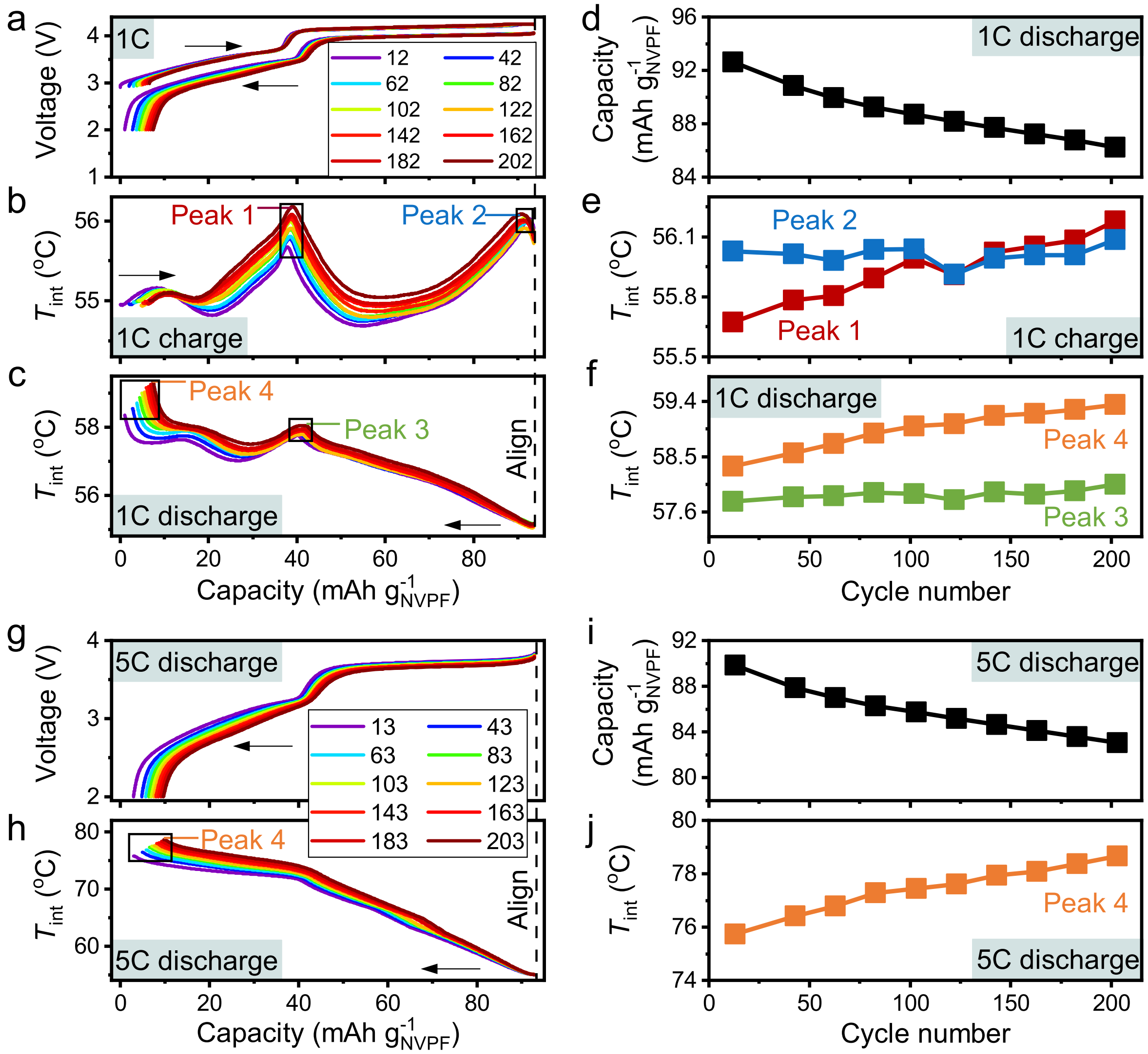

Figure 1. Temperature evolutions upon cell ageing. a-c, The voltage (a) and the internal temperatures (T_{int}) vs capacity at 1 C during the charge (b) and discharge (c) upon ageing in a 55 °C oven. The colours of curves in (a)–(c) vary from purple to red with the increasing cycle number from 12 to 202. (d)–(f), The discharge capacity (d) and the local maxima of temperature (Peaks 1–4) during the charge (e) and discharge (f) as a function of cycle number at 1 C. (g), (h), The evolving voltage (g) and T_{int} (h) vs capacity at 5 C discharge upon ageing. (i), (j), The discharge capacity (i) and the local maxima of temperature (j) vs cycle number at 5 C discharge. In (a)–(c) and (g), (h), the directions of charge or discharge are indicated by arrows, and the curves are aligned at the end of the charge (dash lines).The peaks in (b), (c), (h) are highlighted by solid boxes.

the $\mathrm{d}V/\mathrm{d}Q$ plots, Fig. S1), consistent with our previous report.[27] Therefore, all curves were aligned at the end of the charge for a better comparison. The internal temperature ($T_{internal}$) variations upon ageing during the charge and the discharge were also depicted in Figs. 1b and 1c, respectively. Although the decayed capacity (Figs. 1a, 1d) implies a decrease in the total heating time at each cycle, temperatures visibly increase at most states of charges (SOCs) with the cycling ageing (Figs. 1b, 1c), which implies a higher heat generation rate upon ageing. Nevertheless, the non-uniformity in the temperature variation was still observed across the SOCs (Figs. 1b ,1c). This is most evident during the discharge (Fig. 1c): the temperature increases more with ageing in the lower voltage plateau than in the higher voltage plateau, which coincides with the smaller decrease in capacity in the higher voltage plateau, as seen in Fig. S1. To further quantify the temperature variations, the peak temperatures during the charge (Peaks 1 and 2 in Fig. 1b) and the discharge (Peaks 3 and 4 in Fig. 1c) were plotted as a function of cycle number in Figs. 1e and 1f, respectively. Temperatures at peaks 2 and 3 do not increase much with the cycling ageing, while the temperatures at peaks 1 and 4 do apparently increase. Counter-intuitively, peaks 1 and 3, both of which correspond to the transition between two voltage plateaus, show different variations with ageing. This reminds us that temperature is always history-dependent and that peaks 1 and 3 result from the temperatures accumulated in the lower and upper-voltage plateaus, respectively. Thus, the smaller temperature change in peak 3 than that in peak 1 again emphasizes the relatively intact electrochemistry at the upper-voltage plateau upon ageing.

To test the batteries under extreme conditions, the cells were routinely discharged at 5 C (Fig. 1g) and found that the shapes of temperature curves at 5 C (Fig. 1h) were different from those at 1 C (Fig. 1c). This suggests that the different components (such as entropy and overpotential heat rates as discussed in Fig. 2) in the heat generation respond divergently to the increased current. Nevertheless, more temperature build-up could still be observed at the lower-voltage plateau (Fig. 1h), in agreement with the 1 C results (Fig. 1c). On the other hand, the temperature at 5 C increases by nearly 20 °C in a single discharge (Fig. 1h) compared to ~3 °C at 1 C (Fig. 1c), highlighting the challenges of thermal management in high-power scenarios. Although peak 3 at the transition between two voltage plateaus became difficult to identify (i.e., rapid change in slope), the temperature of peak 4 at the end of discharge and the 5 C discharge capacity against the cycle number were plotted in Figs. 1i,

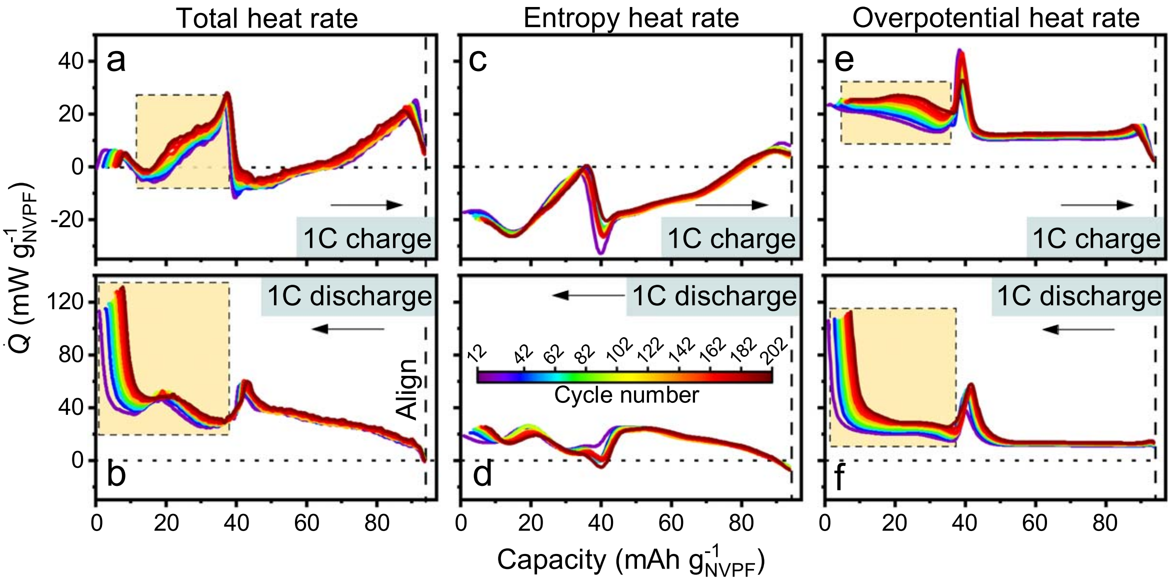

Figure 2. Capacity-dependent heat evolutions upon cell ageing at 1 C. a-f, The absolute evolutions ($\dot{Q}$) of total (a), (b), entropy (c), (d), and overpotential (e), (f) heat rate vs capacity during the charge (a), (c), (e) and the discharge (b), (d), (f) at 1 C. The colours of curves vary from purple to red with the increasing cycle number from 12 to 202, as seen in the inset of d. The dot and dash lines indicate the zero amplitude and the alignment at the end of the charge, respectively. Yellow shadings are used for the regions with significant heat build-up. The directions of charge or discharge are indicated by arrows.

1j. The temperature of peak 4 grew from ∼76 to ∼79 °C at 5 C discharge (Fig. 1j) upon the cycling ageing, which was amplified over that of 1 C (from ∼58 to ∼59 °C, Fig. 1f).

Shortly, the above results show that temperature increases with the cell's cycling ageing and implies different degradations between the two voltage plateaus. Even though temperature directly impacts the reaction kinetics and transport, Eq. 1 reveals that temperature variation (i.e., $\frac{dT}{dt}$) is simultaneously influenced by the cell's heat generation rate ($\dot{Q}$) and heat dissipation rate ($\frac{T_{surface} - T_{ambient}}{R_{out}}$). In other words, temperature measurements are always configuration-dependent. Could the thermal behaviour be measured more intrinsically? While heat dissipation is typically regulated by thermal management (e.g., cooling lines) in the field application, the cell's heat generation ($\dot{Q}$) offers more intrinsic thermal information about the chemistry and design of the cell. Notably, the study of heat evolution with cell ageing is absent in the literature to the authors' knowledge, despite the popularity of isothermal or adiabatic calorimeters for batteries.

Insights from heat analysis into cell ageing.—In addition to the temperature results, the heat evolution with heat capacity contribution was also deciphered by the optical fiber method; see the relevant discussions of Eqs. 1 and 2. Figure 2 shows the ageing-induced variations of total heat generation rate (Figs. 2a, 2b), entropy (Figs. 2c, 2d), and overpotential (Figs. 2e, 2f) heat rate vs capacity during the charge (Fig. 2, top) and discharge (Fig. 2, bottom), which were also aligned at the end of charge. The shapes of heat generation rate curves (Figs. 2a, 2b) are similar to the temperature curves in Figs. 1b, 1c, while the peaks become sharper. These shapes stem from the combination of the entropy term ($\frac{IT}{nF}\left(\frac{ds_+}{dx} - \frac{ds_-}{dx}\right)$) and the overpotential term ($I(V - U)$); see Eq. 2. Notably, the entropy heat rate of NVPF/HC chemistry was mostly endothermic during the charge (Fig. 2c) and exothermic during the discharge (Fig. 2d). The rationale of the opposite sign of entropy heat can be found in the mathematic expression of $\frac{IT}{nF}\left(\frac{ds_+}{dx} - \frac{ds_-}{dx}\right)$, where I, s_+, s_-, and x change the sign between charge and discharge. The opposite entropy heats during the charge and discharge explain the lower total heat generation rate (Figs. 2a, 2b) and temperature (Figs. 1b, 1c) during the charge than those during the discharge.

Turning to the variation with cycle ageing, the heat generation rate increases with the number of cycles in a heterogeneous way at the state of charge: heat generation increases more at low SOCs (yellow shadings in Figs. 2a, 2b). For almost identical SOCs, significant increases in overpotential heat rate with the number of cycles are also observed (yellow shadings in Figs. 2e, 2f). In contrast, the change in magnitude of the entropy heat rate upon cycling ageing is less obvious (Figs. 2c, 2d).

At this point, it is legitimate to wonder why the overpotential shows a SOC-dependent increase during cell ageing. To answer this question, the overpotential were further decomposed into *iR* drop, transport-related overpotential, and quasi-static hysteresis (Fig. 3) corresponding to short, medium, and long relaxation time in the GITT test, respectively (see more details in our previous paper).[12] Note that the overpotential pertaining to the charge transfer interfacial kinetics should also be included by the term of "transport-related overpotential." Remarkably, the overpotential curves of *iR* drop during both charge (Fig. 3b) and discharge (Fig. 3e) were parallel to each other and showed almost no SOC-dependent increases with cycle number, indicating this SOC-dependency of overpotential increase is not due to fast (or high-frequency) processes such as the electrical resistance. Instead, more increase was observed in the low-SOC regions with the transport-related overpotential (yellow shadings in Figs. 3c, 3f) and the quasi-static hysteresis (yellow shading in Fig. 3d). These results suggest an ageing mechanism that largely deteriorates the transport kinetics at the lower-voltage plateau. It is generally believed that the loss of sodium inventory observed by the slippage previously in NVPF or HC is the main ageing mechanism behind the degradation of NVPF/HC chemistry;[28] however, this mechanism alone cannot explain the heterogenous deterioration of transport kinetics in the present case. Therefore, we believe that there must be another ageing mechanisms that have altered the crystalline structure of materials, such as the dissolution of vanadium in NVPF, as we have recently reported.[29] Finally, the structure-related ageing mechanism is also supported by the variation of entropy profiles at the lower-voltage plateau in Figs. 2c, 2d.

Heat deterioration with the cycling ageing.—At this stage, another interesting question is how thermal management should adapt to cell ageing. The mean heat generation rate ($\dot{Q}$) within one

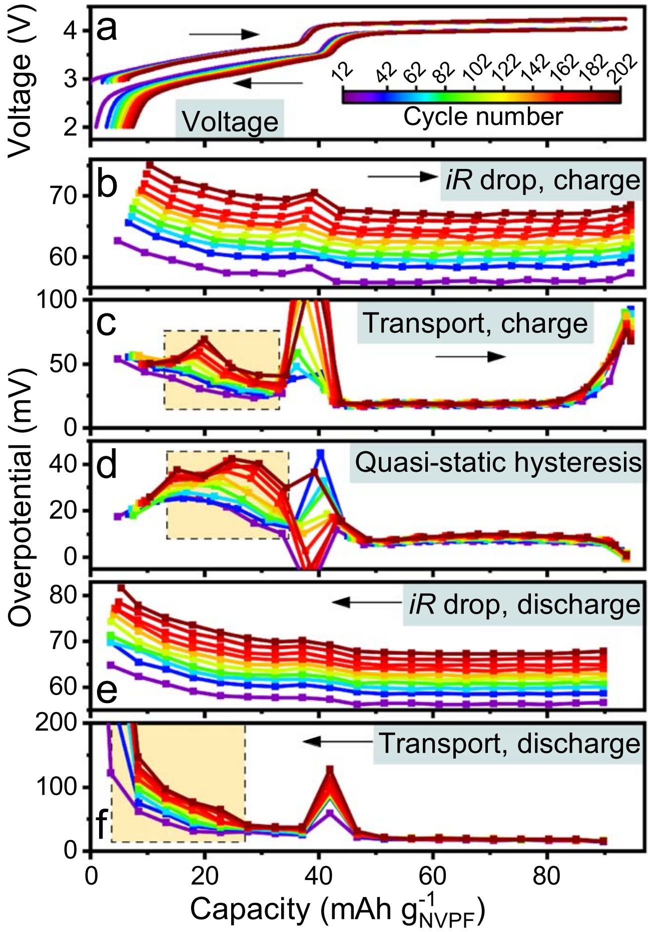

Figure 3. Overpotential decompositions upon cell ageing at 1 C. (a), The voltage vs capacity at 1 C during the charge and discharge upon ageing in a 55 °C oven. (b)–(f), The evolutions of the overpotential components, including *iR* drop (b), (e), transport (c), (f), and quasi-static hysteresis (d) vs capacity during the charge (b), (c) and discharge (e), (f) that are deconvoluted by the GITT test at 1 C. The colours of scatters vary from purple to red with the increasing cycle number from 12 to 202, as seen in the inset of (a), and lines are provided as a guide to the eyes. Yellow shadings are used for the regions with more significant changes. The directions of charge or discharge are indicated by arrows.

charge or discharge was thus calculated in Fig. 4a. Due to the endothermic entropy heat, the mean $\dot{Q}$ values are close to 0 mW g_{NVPF}^{-1} (Fig. 4a, red) during 1 C charging compared to ~30 mW g_{NVPF}^{-1} (Fig. 4a, blue) during the 1 C discharging. The mean $\dot{Q}$ values are elevated to over 300 mW g_{NVPF}^{-1} (Fig. 4a, yellow) when the cell is discharged at 5 C. The 10-fold difference (300/30) between discharges at 1 C and 5 C contradicts the frequently used simplified thermal model ($\dot{Q} \approx I^2R$, leading to 25 times), where entropy is neglected. This contradiction stems from the fact that *iR* alone cannot represent the complex components of heat generation, including entropy, transport-related, and quasi-static hysteresis overpotentials, as shown in Figs. 2 and 3. With regard to the variations of $\dot{Q}$ with cycle number, the mean $\dot{Q}$ of 1 C charge increases at a rate of +0.02 (±0.001) mW g_{NVPF}^{-1} $cycle^{-1}$ (Fig. 4a, red), greater than that of 1 C discharge (+0.01 (±0.001) mW g_{NVPF}^{-1} $cycle^{-1}$, Fig. 4a, blue). Though 0.02 mW g_{NVPF}^{-1} $cycle^{-1}$ seems small, it corresponds to ca. 1% $cycle^{-1}$, which could become considerable after hundreds of cycles. Meanwhile, the mean $\dot{Q}$ of 5 C discharge grows linearly with cycle number at a much higher rate of +0.25 mW g_{NVPF}^{-1} $cycle^{-1}$, corresponding to around 0.1% $cycle^{-1}$.

To better understand the different rates of increase in mean $\dot{Q}$ with cycle number, the average entropy and overpotential heat rate of one discharge or charge were computed as a function of the cycle number in Figs. 4b, 4c. Considering first the 5 C discharge, the mean entropy heat rate becomes more and more endothermic (−0.12 mW g_{NVPF}^{-1} $cycle^{-1}$) with cycle number (Fig. 4b, red). In contrast, the mean overpotential heat rate is increasingly exothermic at a speed of +0.36 mW g_{NVPF}^{-1} $cycle^{-1}$ (Fig. 4b, purple). Consequently, the increase in mean $\dot{Q}$ at 5 C discharge is solely due to the growth of overpotential. At the same time, the decreasing in the mean entropy heat rate (Fig. 4c, yellow) and the increasing overpotential heat rate (Fig. 4c, purple) with the number of cycles are also seen in 1 C discharge, at absolute rates of 0.02 and 0.03 mW g_{NVPF}^{-1} $cycle^{-1}$, respectively. This counterbalance explains why the mean $\dot{Q}$ of 1 C discharge increases very slowly with cycle number (Fig. 4a, blue). Turning to 1 C charge, the mean overpotential heat rate of 1 C charge (Fig. 4c, red), irrespective of the number of cycles, is lower than that of 1 C discharge (Fig. 4c, purple), because the CC-CV scheme leads to a lower average charge C-rate. In addition, the increase of mean overpotential heat rate with cycle number in 1 C charge (Fig. 4c, red, +0.02 mW g_{NVPF}^{-1} $cycle^{-1}$) is also slower than that of 1 C discharge (Fig. 4c, purple, +0.03 mW g_{NVPF}^{-1} $cycle^{-1}$). This difference may be due to the greater growth of transport-related overpotentials of 1 C discharge at the low-SOC regions (yellow shading in Fig. 3f) than that of the 1 C charge (yellow shading in Fig. 3c), which also depends on structural deterioration as discussed later. On the other hand, unlike the 1 C discharge counterpart (Fig. 4c, yellow), the mean entropy heat rate of charge (Fig. 4c, green) does not increase with cycle number, implying exacerbated sodiation-desodiation asymmetry or side reactions arising from the cell ageing mechanisms.

Furthermore, the components of the mean overpotential heat rate at 1 C charge were also computed according to the results from Fig. 3, to show their variations with cycle number in Fig. 4d. In terms of magnitude first, the *iR* drop contributes mostly (~65 mV) to the overpotential heat, while the transport-related and quasi-static hysteresis overpotentials contribute ~35 and ~15 mV, respectively. In terms of rate of increase with the number of cycles, *iR* and transport-related overpotentials increase at a similar rate of +0.06 mV $cycle^{-1}$, while the quasi-static hysteresis overpotential increases relatively slowly at +0.03 mV $cycle^{-1}$.

Enthalpy evolutions upon the ageing.—Another interesting observable that can be derived from the heat measurement is the enthalpy potential (U_H), as defined by the following equation:[12,24,26]

$$U_H = -\frac{\Delta H}{nF} \quad [3]$$

with ΔH being the change of enthalpy (H) of the cell's main reaction. While ΔG can be derived from the equilibrium cell potential, ΔH can be derived from a so-called enthalpy potential (U_H), which could be determined from Eq. 4[12,24,26] by ignoring the heat of mixing and parasitic reactions:

$$U_H = V - \frac{\dot{Q}}{I} \quad [4]$$

In principle, U_H offers purely thermodynamic information without the contamination of kinetics. It is previously explored in our work on anionic redox[26] that one could retrieve a thermodynamic quantity from an out-of-equilibrium (fast) measurement through Eq. 4. The U_H vs capacity curves of charge and discharge are shown in Figs. 5a and 5b, respectively. In line with the previous discussion, the U_H at the upper-voltage plateau remains nearly unchanged with the cycling ageing, while the U_H at low voltages (yellow shadings in Figs. 5a, 5b) has decreased with cycle number in both charge and discharge, suggesting the ΔH changes of low-voltage reactions. To further

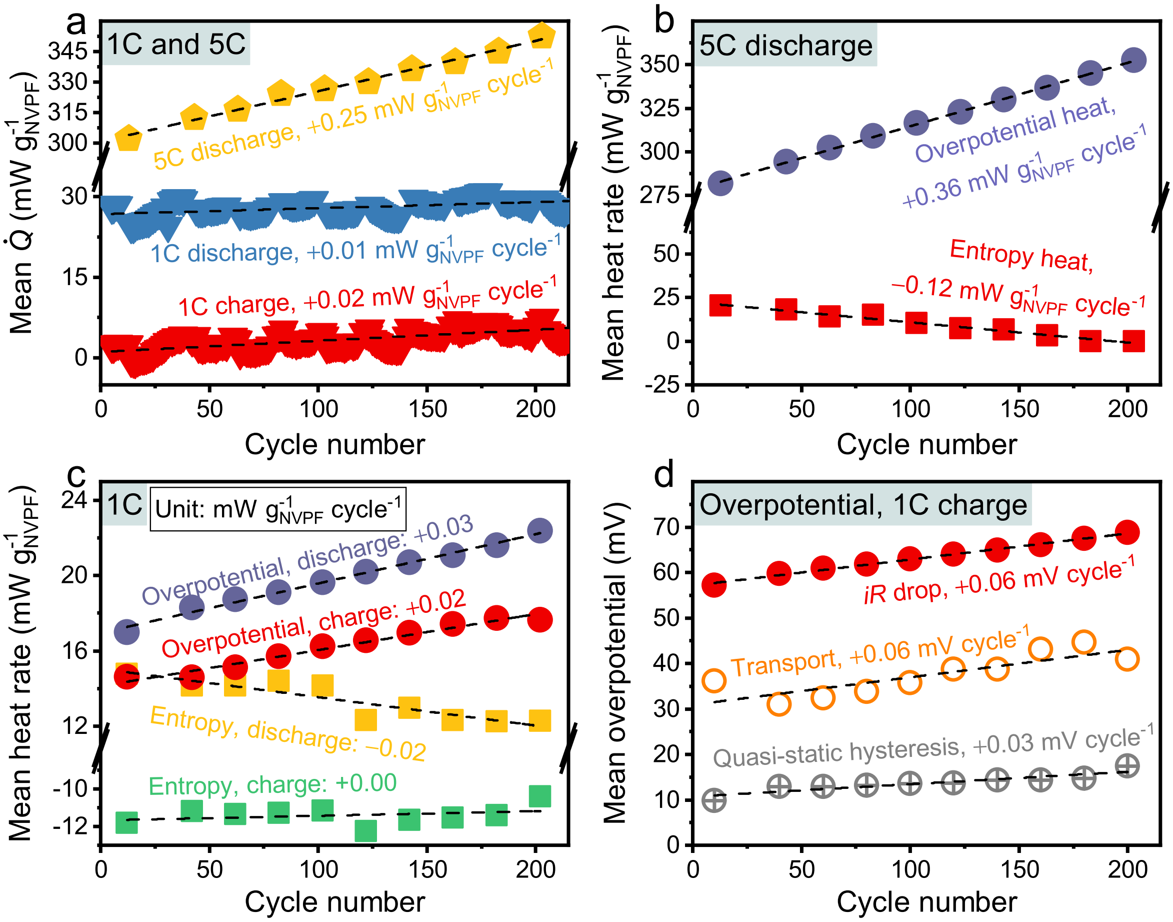

Figure 4. Cycle-dependent heat evolutions upon cell ageing. (a), The mean total heat rate ($\dot{Q}$) of 1 C charge (red, triangle), 1 C discharge (blue, triangle), and 5 C discharge (yellow, pentagon) as a function of cycle number. (b), The deconvoluted overpotential (purple, circle) and entropy (red, rectangle) heat rate as a function of cycle number at 5 C discharge. (c), The deconvoluted overpotential (circle) and entropy (rectangle) heat rate as a function of cycle number during 1 C charge (red and green for overpotential and entropy, respectively) and discharge (purple and yellow for overpotential and entropy, respectively). (d), The deconvoluted overpotential components, including *iR* drop (red, solid circle), transport-related (orange, hollow circle), and quasi-static hysteresis (grey, cross circle) as a function of cycle number that are deconvoluted by the 1 C GITT test. Only the charge part is shown for the sake of the figure length. The dash lines in (a)–(d) are the linear fittings of the data with the slopes indicated.

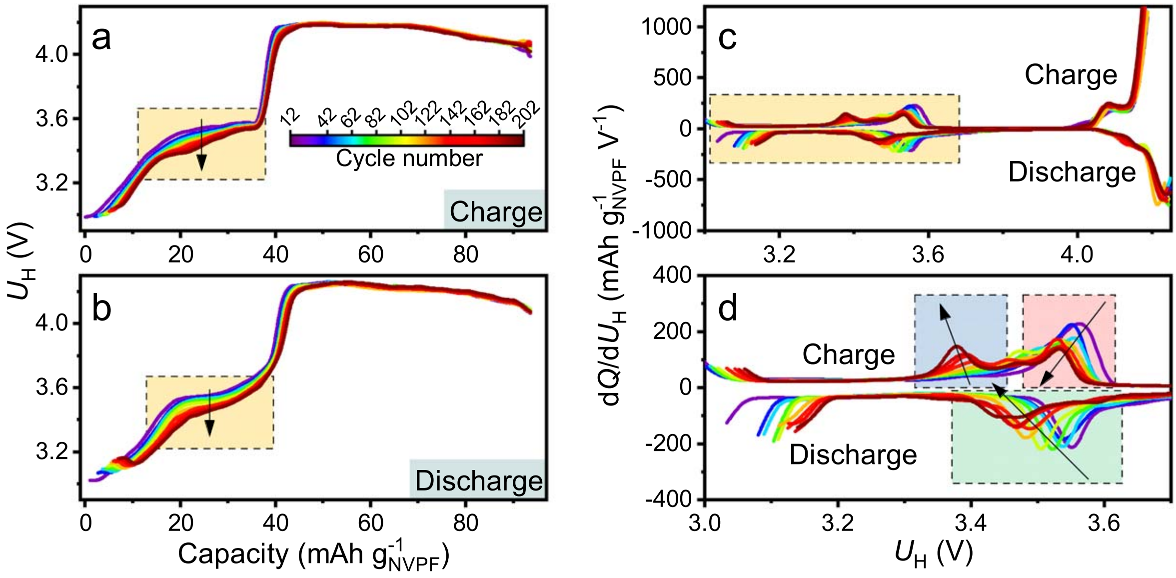

Figure 5. Evolution of enthalpy potential upon cell ageing at 1 C. (a), (b), The enthalpy potential (U_H) vs capacity curves upon ageing during the charge (a) and discharge (b) at 1 C. (c), (d), The dQ/dU_H vs U_H curves upon cycling ageing (c) with the zoomed view of the low-voltage region (d). The arrows serve as guides for the trend to the eyes. The colours of curves vary from purple to red with the increasing cycle number from 12 to 202, as shown in the inset of (a). Note that the points in (c), (d) are connected and plotted by B-spline. Shadings are used to highlight the regions with relatively significant changes.

decode the changes, the dQ/dU_H plot was constructed in Fig. 5c in a similar fashion as for the conventional dQ/dV derivative plots. Zooming in on the low-voltage region (yellow shading in Fig. 5c) during charging, the redox peak near 3.56 V continuously decreases and moves to a lower voltage (red shading in Fig. 5d), while a new redox peak gradually emerges at 3.40 V upon cycling ageing (blue shading in Fig. 5d). Coincidentally, the 3.40 V is close to the redox center of the dissolved vanadium.[29] This is further evidence in support of our hypothesis of a structure-related ageing mechanism. In the zoomed dQ/dU_H plot of the discharge, the redox peak near 3.56 V moves to a lower potential at the same time as it broadens (green shading in Fig. 5d), which is perhaps a convolution of the two peaks as in the charge (or perhaps a single peak decreasing in magnitude while broadening and shifting down to a lower potential).

Comparing ageing fingerprints from quasi- and non-equilibrium quantities.—As mentioned, dQ/dV plot is also frequently used to diagnose the battery ageing,[29] which was thus plotted in Figs. 6a, 6b for comparison to dQ/dU_H. From the amplitude in the unit of mAh g_{NVPF}^{-1} V^{-1}, the peaks of dQ/dU_H were taller and sharper, while those of dQ/dV were broader and less distinguishable at such a high rate of 1 C. Nevertheless, dQ/dV also provide some useful information (Figs. 6a, 6b): Redox peaks are broadened and shifted upward (on charge, red shading in Fig. 6b) and downward (on discharge, green shading in Fig. 6b) because of the overpotential contributions. However, the critical peak at 3.40 V in dQ/dU_H is absent or blurred in the dQ/dV plot, highlighting the sensitivity of dQ/dU_H to cell ageing.

To further examine the advantages of enthalpy potential, the equilibrium potential (U) was estimated by the OCVs from the GITT test, see Fig. S2. Likewise, the dQ/dU curves upon cyclic ageing were computed and plotted in Figs. 6c, 6d. Similar to dQ/dV and dQ/dU_H, the redox peaks at ∼3.55 V during both charge (red shading, Fig. 6d) and discharge (green shading, Fig. 6d) decrease in amplitude and shift to lower voltages progressively. Moreover, a pair of new redox peaks emerge at ∼3.22 V during the charge (blue shading, Fig. 6d) and discharge (purple shading, Fig. 6d), which are insignificant in dQ/dV plots and again underline the superiority of quasi-equilibrium quantities over those measured at a high rate such as 1 C.

For making a more straightforward comparison, the low-voltage regions of all three derivatives are plotted together at around the 12th and 202nd cycles in Figs. 6e, 6f, respectively. In the less aged state at around the 12th cycle (Fig. 6e), the redox peaks of both dQ/dU (blue arrows) and dQ/dU_H (red arrows) are nearly symmetric and center around 3.55 V, while the peaks of dQ/dV (yellow arrows) are separate due to the overpotentials. Furthermore, the peaks' amplitudes of dQ/dU and dQ/dU_H are higher than that of dQ/dV, owing mainly to the considerable non-equilibrium portions in V particularly at a high rate of 1 C. This is consistent with the previous report[30] that

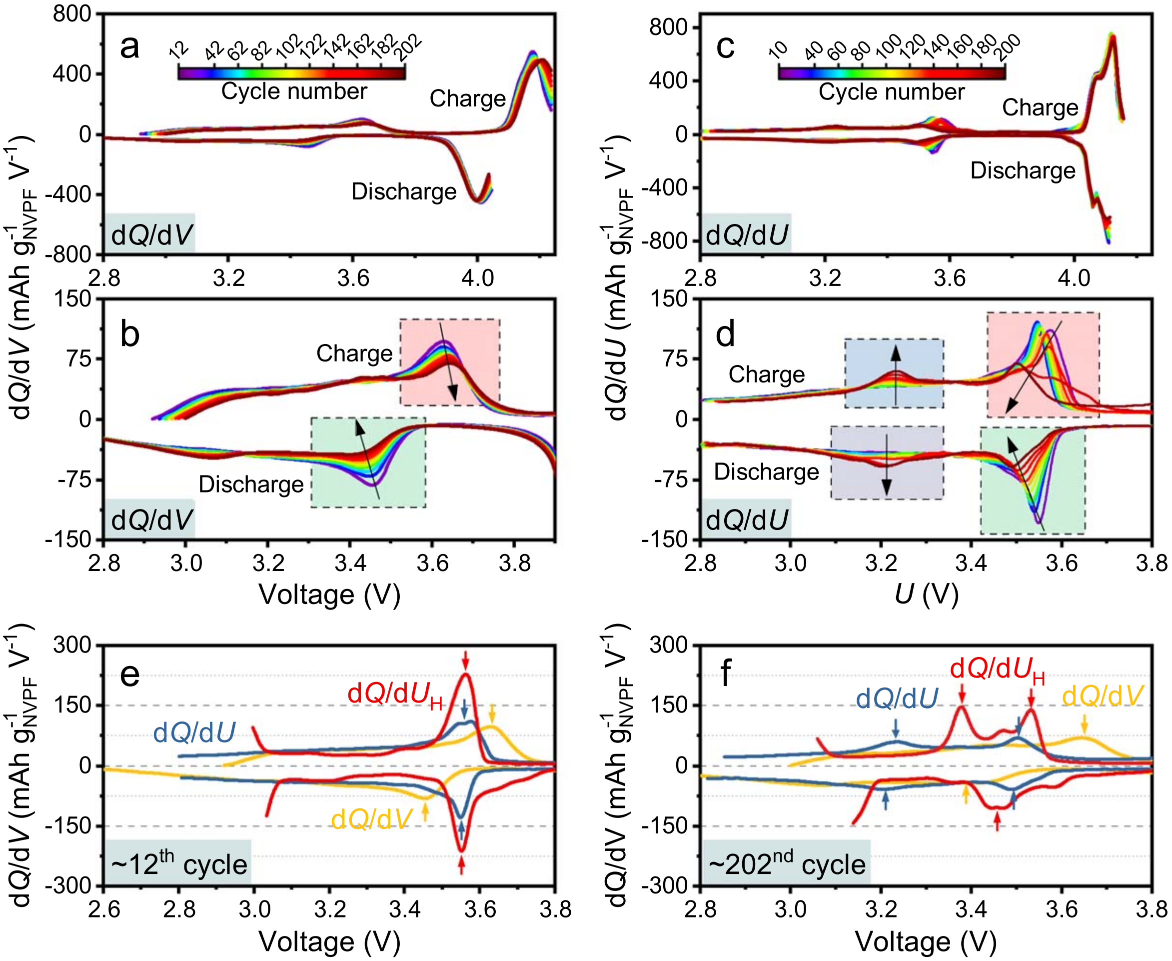

Figure 6. Comparing the dQ/dV plots relying on quasi-equilibrium and non-equilibrium voltages. a,b, The dQ/dV vs voltage curves upon cycling ageing (a) with the zoomed view of the low-voltage region (b). The colours of curves vary from purple to red with the increasing cycle number from 12 to 202 as shown in the inset of a. (c), (d), The dQ/dU vs U curves upon cycling ageing (c) with the zoomed view of the low-voltage region (d). U was estimated by the OCVs during the GITT test; see Fig. S2. The colours of curves vary from purple to red with the increasing cycle number from 10 to 200, as shown in the inset of (c). Shadings in (a)–(d) are used to highlight the regions with relatively significant changes. The arrows in a-d serve as guides for the trend to the eyes. (e), (f), The comparison of quasi-equilibrium dQ/dU (blue) and dQ/dU_H (red) with the non-equilibrium dQ/dV (yellow) at ca. 12th (e) and 202nd (f) cycles. Arrows in e,f indicate the positions of peaks.

the peaks of dQ/dV plots became broader and less intensive at a high rate of 1 C in comparison to those at C/72, where the cell at the extremely low C-rate is approaching the quasi-equilibrium states. Among quasi-equilibrium quantities, the peak amplitude of dQ/dU_{H} is higher than that of dQ/dU (Fig. 6e). Aside from the influence of entropy, this difference in amplitude may stem from the fact that only 20 OCVs were collected in GITT for each charge/discharge (Fig. S2) for the sake of measurement time, which compromises the spectral resolution of dQ/dU and smooths the peaks down.

Turning to the relatively aged state at around the 202nd cycle (Fig. 6f), the intensities of dQ/dV peaks (yellow arrows) were diminished as their breadths expanded, rendering the peaks hardly distinguishable. This concurs with the previous study[30] showing that the number of identifiable peaks decreases upon ageing at 1C, while these peaks remain retrievable at a low rate of C/24 or C/6, which is closer to the equilibrium states. The advantage of equilibrium state functions is further verified by the relatively sharp peaks in dQ/dU (blue arrows, Fig. 6f) and dQ/dU_{H} (red arrows, Fig. 6f). In addition to the peak intensity and positions, the dQ/dU and dQ/dU_{H} curves capture the modified reaction pathways by the emerging additional redox peaks (Fig. 6f), which could pertain to soluble vanadium species[29] or other unknown reactions. Notably, the peak positions of dQ/dU and dQ/dU_{H} become partially different at ∼202nd cycle. This inconsistency can originate from the impact of the entropy term (as in $U_H = U - T\frac{dU}{dT}$), while the low spectral resolution of dQ/dU based on GITT's OCVs can be partly blamed. This again spotlights the high-resolution data of enthalpy potential relying on operando, high-resolution measurements of voltage and heat even at a high C-rate of 1 C. More importantly, this work provides an approach to determine state functions (e.g., enthalpy) that are equilibrium quantities but stem from nonequilibrium measurements, for example, under ageing conditions and at high rates, without time-consuming low-rate or GITT tests.

Conclusions

We demonstrated that fiber Bragg grating sensors and fiber optical calorimetry are useful for tracking the thermal changes (temperature and heat) during cell ageing, which has not been done in previous literature. Combined with the deconvolution methodology, we showed the thermal signals could be highly informative, allowing us not only to explain the origins of temperature/heat deterioration, but also to elucidate the structure-related ageing mechanism via the SOC dependence. We also summarized the average heat release rate during charge/discharge and provided insights into how the thermal management can adapt to the cell ageing of NVPF/HC chemistry, while the same methodology can be easily transposed to other chemistry or cell designs. In addition, we have adopted the enthalpy potential to study the battery ageing mechanism, and we must admit that we were not the first to do so. Yazami et al. used the potentiometric method to access enthalpy and then to study the degradation of graphite and lithium cobalt oxide chemistry.[31] However, using fiber optical calorimetry, we were able to operando collect the enthalpy information without varying furnace temperatures or switching to low C-rates, thus providing high-resolution data for the dQ/dU_{H} analysis. This is a new approach to determining the batteries' state functions (e.g., enthalpy) that are equilibrium quantities but stem from nonequilibrium measurements. Moreover, we proved that the introduction of dQ/dU_{H} provided critical ageing fingerprints, which were hidden in the dQ/dV analysis. The cycle-dependent variations in entropy have also been exploited, revealing interesting features that will form the core of a subsequent article to avoid excessive complexity in the context of this work.

Outlook

In the future, fiber optic sensors can be even more versatile in monitoring cell ageing. For example, the side reactions are often accompanied by outgassing, making it useful to detect pressure or even the gas type/concentration. To this end, we have already demonstrated[12] that the FBG written in microstructured optical fiber can enable the detection of pressure inside the 18650 commercial cells. However, we must realize that other methods (dQ/dV, electrochemical impedance spectroscopy, etc.) also offer the possibility of monitoring the state of health of batteries without providing as much information on the battery's chemical and thermal parameters. Clearly, the wealth of information provided by our method for tracking heat and enthalpy potentials comes with a burden, namely, the complexity of the data analysis. We are working to make our optical method easier to use. In addition, the non-trivial implementation of these measurements will complicate the monitoring of each cell in a pack, so for field application, we have to rely on the digital-twin concept of controlling one cell and applying the results to all others. Overall, there are still many opportunities and uncertainties regarding the application of various fiber optic technologies to different chemistries or cell designs for monitoring various chemical and thermodynamic metrics to improve the quality, reliability, and life (QRL) of the battery system by extending the ageing (e.g., lifetime) of battery cells and maximizing their performances.

Acknowledgments

We thank TIAMAT for kindly providing the NVPF/HC 18650 cells. We acknowledge BATTERY 2030+ funded by the European Union's Horizon 2020 research and innovation program under grant agreement No. 957213, and the funding from the International Balzan Prize Foundation via the 2020 Balzan Prize to Jean-Marie Tarascon. J. H. is also indebted to the Hong Kong University of Science and Technology (Guangzhou) startup grant (G0101000062), the Project of Hetao Shenzhen-Hong Kong Science and Technology Innovation Cooperation Zone (HZQB-KCZYB-2020083), and the National Natural Science Foundation of China (No. 52207230). This work is also funded by Guangzhou Municipal Science and Technology Project (No. 2023A03J0003 and No. 2023A03J0103). Author contributions. J. H. and J.-M. T. conceived the idea and designed the experiments. J. H. performed the electrochemical and optical measurements together with the data analysis thanks to the assistance of P. D., C. G. M, L. A. B., and R. T. J. H. did the thermodynamics analysis with the help of C.D. Lastly, J.H. and J.-M.T. wrote the paper with contributions from C.D. Conflict of interests. The authors declare no competing financial interests.

ORCID

Jiaqiang Huang https://orcid.org/0000-0001-8250-228X
Charles Delacourt https://orcid.org/0000-0001-5241-5441
Laura Albero Blanquer https://orcid.org/0000-0001-7906-4442

References

1. D. Larcher and J. M. Tarascon, *Nat. Chem.*, **7**, 19 (2015).
2. H. E. Melin, M. A. Rajaeifar, A. Y. Ku, A. Kendall, G. Harper, and O. Heidrich, *Science*, **373**, 384 (2021).
3. C. Vaalma, D. Buchholz, M. Weil, and S. Passerini, *Nat. Rev. Mater.*, **3**, 18013 (2018).
4. J.-M. Tarascon, *Joule*, **4**, 1616 (2020).
5. J. Huang, S. T. Boles, and J.-M. Tarascon, *Nat. Sustain.*, **5**, 194 (2022).
6. A. J. Smith, J. C. Burns, X. Zhao, D. Xiong, and J. R. Dahn, *J. Electrochem. Soc.*, **158**, A447 (2011).
7. H. M. Dahn, A. J. Smith, J. C. Burns, D. A. Stevens, and J. R. Dahn, *J. Electrochem. Soc.*, **159**, A1405 (2012).
8. A. J. Louli et al., *Nat. Energy*, **5**, 693 (2020).
9. Z. Deng, Z. Huang, Y. Shen, Y. Huang, H. Ding, A. Luscombe, M. Johnson, J. E. Harlow, R. Gauthier, and J. R. Dahn, *Joule*, **4**, 2017 (2020).
10. A. Louli, L. Ellis, and J. Dahn, *Joule*, **3**, 745 (2019).
11. X. Lu, J.-M. Tarascon, and J. Huang, *eTransportation*, **14**, 100207 (2022).
12. J. Huang et al., *Nat. Energy*, **5**, 674 (2020).
13. J. Huang, L. Albero Blanquer, C. Gervillie, and J.-M. Tarascon, *J. Electrochem. Soc.*, **168**, 060520 (2021).
14. S. Novais, M. Nascimento, L. Grande, M. Domingues, P. Antunes, N. Alberto, C. Leitão, R. Oliveira, S. Koch, and G. Kim, *Sensors*, **16**, 1394 (2016).

15. M. Nascimento, S. Novais, M. S. Ding, M. S. Ferreira, S. Koch, S. Passerini, and J. L. Pinto, *J. Power Sources*, **410**, 1 (2019).
16. G. Yang, C. Leitão, Y. Li, J. Pinto, and X. Jiang, *Measurement*, **46**, 3166 (2013).
17. M. Nascimento, T. Paixão, M. S. Ferreira, and J. L. Pinto, *Batteries*, **4**, 67 (2018).
18. L. Albero Blanquer, F. Marchini, J. R. Seitz, N. Daher, F. Bétermier, J. Huang, C. Gervillié, and J.-M. Tarascon, *Nat. Commun.*, **13**, 1153 (2022).
19. J. Huang, X. Han, F. Liu, C. Gervillié, L. A. Blanquer, T. Guo, and J.-M. Tarascon, *Energy Environ. Sci.*, **14**, 6464 (2021).
20. C. Gervillié-Mouravieff et al., *Nat. Energy*, **7**, 1157 (2022).
21. A. Ganguli, B. Saha, A. Raghavan, P. Kiesel, K. Arakaki, A. Schuh, J. Schwartz, A. Hegyi, L. W. Sommer, and A. Lochbaum, *J. Power Sources*, **341**, 474 (2017).
22. T. Waldmann, M. Wilka, M. Kasper, M. Fleischhammer, and M. Wohlfahrt-Mehrens, *J. Power Sources*, **262**, 129 (2014).
23. C. Forgez, D. V. Do, G. Friedrich, M. Morcrette, and C. Delacourt, *J. Power Sources*, **195**, 2961 (2010).
24. K. E. Thomas and J. Newman, *J. Electrochem. Soc.*, **150**, A176 (2003).
25. L. Downie, S. Hyatt, and J. Dahn, *J. Electrochem. Soc.*, **163**, A35 (2016).
26. G. Assat, S. L. Glazier, C. Delacourt, and J.-M. Tarascon, *Nat. Energy*, **4**, 647 (2019).
27. G. Yan, R. Dugas, and J.-M. Tarascon, *J. Electrochem. Soc.*, **165**, A220 (2018).
28. P. Desai, J. Huang, H. Hijazi, L. Zhang, S. Mariyappan, and J. M. Tarascon, *Adv. Energy Mater.*, **11**, 2101490 (2021).
29. P. Desai, J. Forero-Saboya, V. Meunier, G. Rousse, M. Deschamps, A. Abakumov, J.-M. Tarascon, and S. Mariyappan, *Energy Storage Mater.*, **57**, 102 (2022).
30. A. Fly and R. Chen, *J. Energy Storage*, **29**, 101329 (2020).
31. K. Maher and R. Yazami, *J. Power Sources*, **247**, 527 (2014).